J. Fluid Mech. (1994), *vol.* 279, *pp.* 351–375

A numerical study of three-dimensional vortex ring instabilities: viscous corrections and early nonlinear stage

By KARIM SHARIFF[1], ROBERTO VERZICCO[2] AND PAOLO ORLANDI[2]

[1] NASA-Ames Research Center, Moffett Field, CA 94035, USA
[2]Università di Roma "La Sapienza" Dipartimento di Meccanica e Aeronautica, via Eudossiana n° 18, 00184 Roma, Italy

(Received 20 September 1993 and in revised form 31 May 1994)

Finite-difference calculations with random and single-mode perturbations are used to study the three-dimensional instability of vortex rings. The basis of current understanding of the subject consists of a heuristic inviscid model (Widnall, Bliss & Tsai 1974) and a rigorous theory which predicts growth rates for thin-core uniform vorticity rings (Widnall & Tsai 1977). At sufficiently high Reynolds numbers the results correspond qualitatively to those predicted by the heuristic model: multiple bands of wavenumbers are amplified, each band having a distinct radial structure. However, a viscous correction factor to the peak inviscid growth rate is found. It is well described by the first term, $1 - \alpha_1(\beta)/Re_S$, for a large range of Re_S. Here Re_S is the Reynolds number defined by Saffman (1978), which involves the curvature-induced strain rate. It is found to be the appropriate choice since then $\alpha_1(\beta)$ varies weakly with core thickness β. The three most nonlinearly amplified modes are a mean azimuthal velocity in the form of opposing streams, an $n = 1$ mode (n is the azimuthal wavenumber) which arises from the interaction of two second-mode bending waves and the harmonic of the primary second mode. When a single wave is excited, higher harmonics begin to grow successively later with nonlinear growth rates proportional to n. The modified mean flow has a doubly peaked azimuthal vorticity. Since the curvature-induced strain is not exactly stagnation-point flow there is a preference for elongation towards the rear of the ring: the outer structure of the instability wave forms a long wake consisting of n hairpin vortices whose waviness is phase shifted π/n relative to the waviness in the core. Whereas the most amplified linear mode has three radial layers of structure, higher radial modes having more layers of radial structure (hairpins piled upon hairpins) are excited when the initial perturbation is large, reminiscent of visualization experiments on the formation of a turbulent ring at the generator.

1. Introduction

Among the many mechanisms by which a vortex may become unstable, the present work is concerned with an inviscid instability which occurs when a vortex is strained, either by other vortices or, as in the case of a vortex ring, by other portions of the curved vortex itself. It is exemplified for long waves by the Crow (1970) instability of aircraft trailing vortices, for intermediate wavenumbers by either the Widnall

instability of vortex rings or the translative instability of Pierrehumbert & Widnall (1982) in mixing layers, and for very short waves by the Pierrehumbert (1986) and Bayly (1986) instability: Saffman (1988) discusses all three in a unified way. In the region of the parameter space accessible in vortex ring experiments (relatively low Reynolds numbers and not too thin cores) it is the intermediate wavenumber instability that has been observed. A heuristic but useful way of understanding all three forms of the instability, expounded in Widnall, Bliss & Tsai (1974, hereafter WBT), is that a rectilinear vortex has only neutral inertial waves which rotate around the core: those waves that rotate with sufficiently small angular velocity are amplified when a straining field is imposed. Turbulent vortex rings form either after undergoing such an instability (Maxworthy 1977) or soon after fluid is ejected at a pipe or orifice via a process which is less clear Glezer (1988).

Despite the success of the WBT model in predicting the observed number of waves and the rigorous treatment of Widnall & Tsai (1977, hereafter WT) which predicts the growth rate, there remain a number of important unresolved issues and we believe that they may be addressed by numerical simulation of the Navier–Stokes equations. Three goals were set at the outset: to investigate some open questions regarding the linear phase of the instability, to investigate the nonlinear phase of the instability and the transition to turbulence, and to study some mechanisms which may be important during the formation of a turbulent ring at a vortex generator. This contribution is a partial fulfillment of these goals. The next section supplies some details of the numerical method and §3 discusses the initial conditions and parameter space explored. Section 4 presents results and is divided into sub-sections. The first sub-section considers a random perturbation and illustrates the basic features of the instability. By presenting growth rates and mode shapes it first shows that the predictions of the heuristic theory remain qualitatively correct even for thick cores and then discusses some early nonlinear effects such as the rapid growth of low-order azimuthal modes. This sub-section also serves as a pedagogical platform for introducing required background terminology.

The work in § 4.2 investigates why the peak growth rate in § 4.1 is smaller than the theoretical value. Several runs at different Reynolds numbers and initial core sizes are performed to show that of all the possible contributors to the difference, viscosity is the main one for the range of Reynolds numbers considered. The conclusions receive support from the analysis of Landman & Saffman (1987) for the elliptic streamline flow. The time of initial waviness and wave breaking as a function of piston Reynolds number in the experiments of Liess & Didden (1976) is considered. It is shown that Reynolds number effects during the formation of the ring and in the development of the mean core structure are alone sufficient (i.e. using *inviscid* non-rotating mode growth rates) to predict the slowing of the instability with decreasing piston Reynolds number. Therefore such experimental data are not by themselves indicative of a direct viscous effect on growth rates.

Sub-section 4.3 considers an initial perturbation consisting of a single azimuthal Fourier mode. In addition to the Gaussian basic state used in previous sections, an 'equilibrated' basic state is also considered. At the Reynolds number considered, only minor differences in the evolution of modal energies during the transient are detected. Even with the use of equilibrated initial conditions an elongated wake structure is formed indicating that it is due to the instability rather than due to the wake formed as a result of axisymmetric unsteadiness.

In the final sub-section a case of large perturbation is briefly presented motivated by the consideration that this may describe a state after other instability mechanisms

have developed such as the Kelvin–Helmholtz instability, centrifugal or inflectional instability due to ingestion of opposite-signed vorticity during ring formation or a Lin–Corcos (1984) collapse of axial and radial vorticity in a stretched vortex layer. It is found that a wake structure with many layers of hairpin vortices is formed, reminiscent of the flow visualization experiments of the formation of turbulent rings (Glezer 1988).

The paper closes with a discussion of experimental observations which remain unexplained and plans for investigation into the later stages of transition.

2. Numerical scheme

The incompressible Navier–Stokes equations are solved using primitive variables. It is well recognized that both in Cartesian (Harlow & Welch 1965) and in general curvilinear coordinates (Orlandi 1989) it is convenient to use staggered velocities, i.e. to locate each velocity component at the centre of the cell face normal to that component, and to locate the pressure at the centre of the cell. This gives the most compact form for the discrete divergence and gradient operators, gives well-structured matrices and readily yields a solenoidal velocity field to within round-off error.

We employ cylindrical coordinates and introduce the quantities

$$q_\theta = v_\theta, \quad q_r = r v_r, \quad q_z = v_z. \tag{2.1}$$

As will be discussed later, use of the quantity q_r simplifies the treatment of the region near $r = 0$. The Navier–Stokes equations then become

$$\frac{\mathrm{D}q_\theta}{\mathrm{D}t} = -\frac{1}{r}\frac{\partial p}{\partial \theta} + \frac{1}{Re}\left[\frac{\partial}{\partial r}\left(\frac{1}{r}\frac{\partial r q_\theta}{\partial r}\right) + \frac{1}{r^2}\frac{\partial^2 q_\theta}{\partial \theta^2} + \frac{\partial^2 q_\theta}{\partial z^2} + \frac{2}{r^3}\frac{\partial q_r}{\partial \theta}\right], \tag{2.2a}$$

$$\frac{\mathrm{D}q_r}{\mathrm{D}t} = -r\frac{\partial p}{\partial r} + \frac{1}{Re}\left[r\frac{\partial}{\partial r}\left(\frac{1}{r}\frac{\partial q_r}{\partial r}\right) + \frac{1}{r^2}\frac{\partial^2 q_r}{\partial \theta^2} + \frac{\partial^2 q_r}{\partial z^2} - \frac{2}{r}\frac{\partial q_\theta}{\partial \theta}\right], \tag{2.2b}$$

$$\frac{\mathrm{D}q_z}{\mathrm{D}t} = -\frac{\partial p}{\partial z} + \frac{1}{Re}\left[\frac{1}{r}\frac{\partial}{\partial r}\left(r\frac{\partial q_z}{\partial r}\right) + \frac{1}{r^2}\frac{\partial^2 q_z}{\partial \theta^2} + \frac{\partial^2 q_z}{\partial z^2}\right], \tag{2.2c}$$

where

$$\frac{\mathrm{D}q_\theta}{\mathrm{D}t} \equiv \frac{\partial q_\theta}{\partial t} + \frac{1}{r}\frac{\partial q_\theta q_r}{\partial r} + \frac{1}{r}\frac{\partial q_\theta^2}{\partial \theta} + \frac{\partial q_\theta q_z}{\partial z} + \frac{q_\theta q_r}{r^2}, \tag{2.2d}$$

$$\frac{\mathrm{D}q_r}{\mathrm{D}t} \equiv \frac{\partial q_r}{\partial t} + \frac{\partial}{\partial r}\left(\frac{q_r^2}{r}\right) + \frac{\partial}{\partial \theta}\left(\frac{q_\theta q_r}{r}\right) + \frac{\partial q_r q_z}{\partial z} - q_\theta^2, \tag{2.2e}$$

$$\frac{\mathrm{D}q_z}{\mathrm{D}t} \equiv \frac{\partial q_z}{\partial t} + \frac{1}{r}\frac{\partial q_r q_z}{\partial r} + \frac{1}{r}\frac{\partial q_\theta q_z}{\partial 0} + \frac{\partial q_z^2}{\partial z}. \tag{2.2f}$$

The numerical scheme used is described in detail in Verzicco & Orlandi (1993); here we summarize the main features. Second-order central differences are used in all directions. Energy is conserved in the absence of viscosity and time-differencing errors. Time advancement is performed based on the fractional step method of Kim & Moin (1985). The equations are provisionally advanced with the pressure at the previous time step and this results in a velocity field which is non-solenoidal. A quantity Φ, similar to the pressure, is then introduced to obtain a velocity field which is solenoidal. In the present method, a multi-step scheme, in particular the third-order Runge–Kutta method of Wray (1987) is used for the nonlinear terms. This requires the calculation of Φ at each sub-step. The quantity Φ satisfies an elliptic equation which does not require boundary conditions. The elliptic equation is solved by FFTs in the

azimuthal and axial directions, using second-order-accurate modified wavenumbers. The solution in the radial direction is reduced to the inversion of a tridiagonal matrix. This procedure is very efficient and obtains a divergence-free velocity field to within round-off errors. The amount of CPU time required to calculate Φ is less than the CPU time necessary to perform the advancement sub-step.

The coordinate system is singular at $r = 0$. The advantage of using the quantity $q_r = rv_r$ is that on a staggered mesh only q_r needs to be evolved at $r = 0$ and its definition forces it to vanish there. The only term which requires a treatment at $r = 0$ different from the interior scheme is the following viscous term:

$$\left(\frac{\partial}{\partial r}\frac{1}{r}\frac{\partial r q_\theta}{\partial r}\right)_{1/2} = -\frac{1}{r^2}\frac{\partial r q_\theta}{\partial r} + \frac{1}{r}\frac{\partial^2 r q_\theta}{\partial r^2}$$

$$= -\frac{1}{r_{1/2}^2}\frac{(rq_\theta)_1 - 0}{\Delta r} + \frac{1}{r_{1/2}}\left[\frac{(rq_\theta)_{3/2} - (rq_\theta)_{1/2}}{(\Delta r)^2} - \frac{(rq_\theta)_{1/2} - 0}{\frac{1}{2}(\Delta r)^2}\right], \quad (2.3)$$

in which the last difference quotient is one-sided (first order). Only the radial indices are written in (2.3) and the 1/2 indices refer to locations at the centre of an (r, θ) face where the quantity rq_θ is stored on a staggered mesh.

A uniform grid in a finite domain is used. At $r = L_r$ the condition of an inviscid wall is imposed and periodic boundary conditions are employed in the axial direction with period length L_z.

3. Initial conditions and run parameters

3.1. *Basic states*

For most of the cases the unperturbed azimuthal vorticity is simply a Gaussian function of distance from the centre of the core:

$$\left.\begin{aligned} \omega_\theta(t=0) &= \frac{\Gamma}{\pi\sigma_o^2}\mathrm{e}^{-(s/\sigma_o)^2}, \\ s^2 &\equiv z^2 + (r-R)^2, \end{aligned}\right\} \quad (3.1)$$

superposed with a Gaussian of the opposite vorticity centred at $(0, -R)$ in order to make the vorticity vanish at the axis. Here σ_o and R are the initial core radius and toroidal radius of the ring, respectively. For thin rings, the Gaussian maintains its form while its core size spreads as $\sigma^2(t) = \sigma_o^2 + 4\nu t$ (Saffman 1970). However, as σ_o/R increases, curvature effects will be felt and the initial condition (3.1) will not be steady. For the largest core to ring radius ratio of $\sigma_o/R = 0.4131$ considered in this study (3.1) is not a steady state. For core rotation frequencies not small compared to the growth rate, unsteadiness would act as parametric forcing on the instability waves. In order to rule out that some aspects of the observed results are a peculiarity of the unsteadiness an equilibrated vorticity is also briefly considered. A Gaussian core is evolved axisymmetrically until it adjusts to a state of near inviscid equilibrium. The actual procedure consists of evolving the Gaussian core for $80R^2/\Gamma$ time units at a higher Γ/ν of 15000 to prevent the core from becoming too thick, followed by evolution at $\Gamma/\nu = 5500$ for $20R^2/\Gamma$ time units. Figure 1 verifies that this procedure results in satisfaction of the condition for inviscid steadiness that, in a reference frame moving with the vortex, ω_θ/r be some function of the Stokes streamfunction, ψ. The observed functional relationship should be contrasted with the linear relationship that seems to be preferred in planar flow (Leith 1984; Couder & Basdevant 1986).

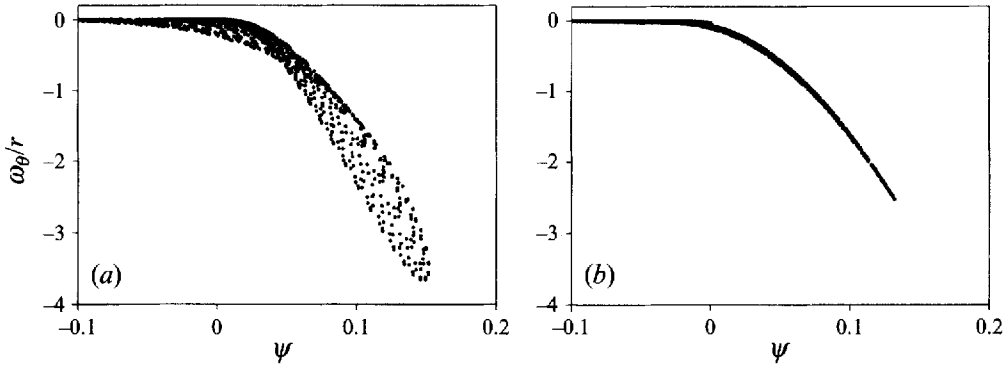

FIGURE 1. Scatter plots of azimuthal vorticity *vs.* Stokes streamfunction at all the grid points ($\sigma_o = 0.4131$). (*a*) Gaussian initial condition. (*b*) Equilibrated initial condition.

3.2. *Initial perturbation*

To first specify the azimuthal vorticity imagine vortex lines to be radially displaced to $r'(\theta)$ from their unperturbed position r_o:

$$r'(\theta) = r_o\,[1 + \epsilon g(\theta)]\,. \tag{3.2}$$

The space curves describing the vortex lines and the unit tangent are

$$\boldsymbol{x} = r'(\theta)\,[\cos\theta\hat{\boldsymbol{x}} + \sin\theta\hat{\boldsymbol{y}}]\,, \quad \hat{\boldsymbol{t}} = \frac{\partial \boldsymbol{x}}{\partial\theta}\Big/\Big|\frac{\partial \boldsymbol{x}}{\partial\theta}\Big|\,. \tag{3.3}$$

Two types of perturbations are considered. In one $g(\theta)$ is a single sine wave and in the other $g(\theta)$ is a sum of Fourier modes with unit amplitudes and random phases. The angle μ between the perturbed and unperturbed vortex lines is given by

$$\cos\mu = \hat{\boldsymbol{t}}\cdot\hat{\boldsymbol{\theta}}, \text{ where } \hat{\boldsymbol{\theta}} = -\sin\theta\hat{\boldsymbol{x}} + \cos\theta\hat{\boldsymbol{y}}. \tag{3.4}$$

Let $\chi(z,r)$ denote the axisymmetric basic state vorticity (either Gaussian or equilibrated). We first specify ω_θ of the perturbed field by imagining $\chi(z,r)$ to be the total vorticity pointing along the tangent to the perturbed vortex lines:

$$\omega_\theta(z,r',\theta) = \chi(z,r)\cos\mu(\theta). \tag{3.5}$$

The axial vorticity is set to zero since the toroidal axis of the ring is assumed to be displaced only radially. The radial vorticity is then obtained by requiring the vorticity field to be divergence free. Since $\omega_z = 0$ this gives

$$\omega_r = -\frac{1}{r}\int_0^r \frac{\partial\omega_\theta}{\partial\theta}\mathrm{d}\rho. \tag{3.6}$$

For the case of a random perturbation, the procedure was slightly different: the axisymmetric vorticity field is considered to be radially displaced but not turned towards the tangent, i.e. $\cos\mu$ is set to 1 in (3.5).

3.3. *Run parameters*

Simulation results are made non-dimensional using the initial circulation Γ and toroidal radius R. The computational domain for random perturbation cases is $(L_z, L_r, L_\theta) = (6R, 4R, 2\pi)$. When a single azimuthal mode n is excited, the computation is performed in the smaller domain $L_\theta = 2\pi/n$. Axial periodicity and the inviscid wall are expected to make a negligible difference compared to an unbounded ring. With

Case	Basic state	σ_o	Γ/ν	Modes excited	ϵ	$N_\theta \times N_r \times N_z$	Δt	t_{final}
1	Gaussian	0.4131	5500	[1,24]	0.0002	$97 \times 97 \times 129$	0.05	90
2	Gaussian	0.4131	4000	[1,32]	0.0002	$129 \times 129 \times 129$	0.05	90
3	Gaussian	0.4131	3000	[1,32]	0.0002	$129 \times 129 \times 129$	0.05	90
4	Gaussian	0.4131	2000	[1,32]	0.0002	$129 \times 129 \times 129$	0.05	90
5	Gaussian	0.4131	1200	[1,32]	0.0002	$129 \times 129 \times 129$	0.05	90
6	Gaussian	0.3099	10000	[1,32]	0.00009	$129 \times 129 \times 129$	0.05	89.75
7	Gaussian	0.3099	7000	[1,32]	0.00009	$129 \times 129 \times 129$	0.05	90
8	Gaussian	0.3099	5500	[1,32]	0.00009	$129 \times 129 \times 129$	0.05	90
9	Gaussian	0.3099	4000	[1,32]	0.00009	$129 \times 129 \times 129$	0.05	90
10	Gaussian	0.3099	3000	[1,32]	0.00009	$129 \times 129 \times 129$	0.05	90
11	Gaussian	0.3099	2000	[1,32]	0.00009	$129 \times 129 \times 129$	0.05	90
12	Gaussian	0.2066	5500	[1,32]	0.00009	$129 \times 129 \times 129$	0.05	90
13	Gaussian	0.2066	4000	[1,32]	0.00009	$129 \times 129 \times 129$	0.05	90
14	Gaussian	0.4131	5500	5	0.00016	$65 \times 97 \times 129$	0.10	90
15	Equlibrated	0.4131	5500	5	0.00016	$65 \times 97 \times 129$	0.10	100
16	Equlibrated	0.4131	5500	5	0.02	$65 \times 97 \times 129$	0.10	50
17	Gaussian	0.4131	5500	5	0.02	$65 \times 97 \times 129$	0.10	50
18	Gaussian	0.4131	5500	5	0.02	$97 \times 129 \times 129$	0.05	60

TABLE 1. Run parameters

the help of the streamfunction of a ring of zero cross-section (a valid assumption for widely separated rings) inside a tube (Brasseur & Chang 1980) we find that the extraneous strain rate induced by an infinite array of such rings is, in the worst case, 2% of the strain rate (due to curvature of the ring itself) which drives the instability.

Table 1 provides run parameters for the cases considered. Three initial core sizes, σ_o, referred to as full, 3/4 and half cores are considered. Some of the Reynolds numbers may seem large for the spatial resolutions employed. In a scheme such as ours which conserves energy in the inviscid limit, loss of resolution is usually indicated by energy pile-up near the cut-off scale and we ensured that this does not happen for the highest Reynolds number case (Case 6).

In order to make estimates from the available theoretical results for a uniform vorticity profile, effective core sizes are defined. For adapting theoretical results for the number of waves and growth rates, the distance, $a_1 = 1.12141\sigma_o$, where the tangential velocity is maximized, is used. This choice is motivated by Saffman's (1978, hereafter S78, p. 630) observation that, for a particular family of profiles, the wavenumber for non-rotating waves on a rectilinear vortex varies less when normalized by a_1 than when normalized by the speed-effective core size a_e (i.e. the core size of the uniform-vorticity ring which matches the speed of Gaussian ring). Furthermore, the eigenvalue problem for rotation rate was solved numerically for the Gaussian profile. Whereas the wavenumbers for the non-rotating second and third modes for uniform vorticity are $ka_1 = 2.51$ and 4.35, they are $k\sigma_o = 2.26$ and 3.96 for the Gaussian profile giving effective core sizes of $1.11\sigma_o$ and $1.10\sigma_o$, respectively. †

Table 2 provides some inviscid parameters. To aid interpretation of time sequences an eddy turnover time, τ_e, defined to be the period of revolution of a particle at radius a_1 in the Gaussian profile, and t_D, the time in which the ring travels one ring

† Generality is not implied in these observations. There are profiles in the literature which attain a maximum of tangential velocity at the core boundary but which have subtantially different values of the non-rotating wavenumbers than the uniform-vorticity core.

σ_o	τ_e	τ_D	α_{WT2}	α_{WT3}
0.2066	2.96	8.11	0.1601	0.1542
0.3099	6.67	9.33	0.1307	0.1246
0.4131	11.8	10.4	0.1092	0.1030

TABLE 2. Inviscid parameters

Case	Re_S	Re_p	Re_D	L/D_e	t_p
1	87.3	4565	2106	2.75	140.0
2	63.5	3320	1531	2.75	102.0
3	47.6	2490	1149	2.75	76.7
4	31.7	1660	766	2.75	51.0
5	19.0	995.9	459	2.75	30.6
6	110.0	10090	4286	1.53	144.0
7	77.0	7060	3000	1.53	101.0
8	60.5	5547	2357	1.53	79.0
9	44.0	4034	1714	1.53	57.4
10	33.0	3026	1286	1.53	43.1
11	22.0	2017	857	1.53	28.7
12	34.0	7117	2712	0.726	35.1
13	24.8	5176	1973	0.726	25.5
14–18	87.3	4565	2106	2.75	140.0

TABLE 3. Additional parameters

diameter, are provided. Both quantities are based on initial properties of the ring. The quantity α_{WT2} is the growth rate of a non-rotating second-radial mode from the WT theory:

$$\alpha_{WT2} = \frac{\Gamma}{4\pi R^2}\left[\left(0.856\log\left(\frac{8R}{a_1}\right) - 0.9102\right)^2 - 0.4535\right]^{1/2}, \tag{3.7}$$

which is valid for thin cores. Note that due to an error in applying their table 1 and equation (8.13) the value of the last coefficient in equation (9.2) of WT should be 0.4535 rather than 0.1138. Similarly, α_{WT3} denotes the growth rate of the third radial mode.

To provide an idea of how much viscous core spreading will affect the instantaneous wavenumber, n, of the most amplified wave, table 4 (second column) gives n corresponding to the second radial mode at $t = 0, 45$, and 90, rounded to the nearest integer, i.e.

$$n(t) = \frac{2.51R}{1.12141\sigma(t)}, \tag{3.8}$$

where

$$\sigma^2(t) = \sigma_o^2 + 4\nu t. \tag{3.9}$$

To guide (roughly) the placing of the simulations within the parameter space of existing experiments, table 3 provides estimates of parameters for a tube-type apparatus using the formulae in S78. One first needs to match, in some way, the Gaussian profile with the hypergeometric profile predicted by the model of self-similar vortex sheet roll-up with viscosity. The shape of the profile has two parameters: a core

size, a, beyond which the vorticity vanishes and $\hat{\epsilon}$, which characterizes its peakiness or relative inner core size. It is related to the core sizes a_e and a_1 by

$$\frac{a_e}{a_1} = \frac{0.47 + 0.63\hat{\epsilon}}{1.45\hat{\epsilon}}. \tag{3.10}$$

Using the value for the Gaussian profile on the left-hand side gives $\hat{\epsilon} = 0.416$. That this is a reasonable value is indicated by the fact that the corresponding hypergeometric profile has $ka_1 = 2.43$ for a non-rotating second mode whereas the Gaussian profile has $ka_1 = 2.53$.

To estimate L/D_e, the piston stroke to exit diameter ratio, start with the identity

$$\frac{a_e}{R} = 2\frac{a_e}{a}\frac{a}{D_e}\frac{D_e}{2R}, \tag{3.11}$$

where a_e is the speed-effective core size ($= 1.3607\sigma_o$ for the Gaussian profile). Saffman provides estimates for each of the factors on the right: †

$$\frac{a_e}{a} = 0.47 + 0.63\hat{\epsilon}, \quad \frac{a}{D_e} = 0.28\left(\frac{L}{D_e}\right)^{2/3}, \quad \frac{D_e}{2R} = \left[1 + 0.22\left(\frac{L}{D_e}\right)^{2/3}\right]^{-1}, \tag{3.12}$$

which may be substituted into (3.11)) and solved for L/D_e. Saffman's expression for circulation gives the piston Reynolds number as

$$Re_p \equiv \frac{U_p D_e}{\nu} = \frac{1}{0.86}\left(\frac{L}{D_e}\right)^{-1/3}\frac{\Gamma}{\nu}, \tag{3.13}$$

where U_p is the piston speed. Glezer (1988) has determined the region in the L/D_e and Γ/ν plane which leads to initially turbulent rings. Although he did not employ a tube-type apparatus for which the above estimates are appropriate, it is worth stating that the present values fall in the non-turbulent region of his transition map.

For laboratory rings $\hat{\epsilon}$ depends on Reynolds number and time, t, from the start of the piston motion:

$$\hat{\epsilon}^2 = 4\nu t/a^2. \tag{3.14}$$

According to S78 (his figure 3) the 0.416 fit to the Gaussian profile is close to the values attained by rings at the onset of waviness in the range of Re_p of the present runs. Table 3 provides the time, t_p (in simulation units), from the start of piston motion at which the assumed value of $\hat{\epsilon}$ would be realized. Future numerical work might benefit from first considering experimental parameters and then using the appropriate hypergeometric profile.

In addition to Re_D, based on ring speed and diameter, table 3 gives a Reynolds number which we shall find is more relevant in determining the character of the instability. It was first defined in S78 and is the ratio of the strain rate, e, due to curvature which drives the instability and the scale for the viscous damping rate:

$$Re_S = \frac{ea_1^2}{\nu}. \tag{3.15}$$

† A factor of 2 missing in Saffman's equation (3.3a) is inconsequential since the coefficient 0.22 in equation (15c) is a fit to experimental data. Coefficients provided later by Pullin (1986) and Didden (1979) are more accurate only for short stroke lengths.

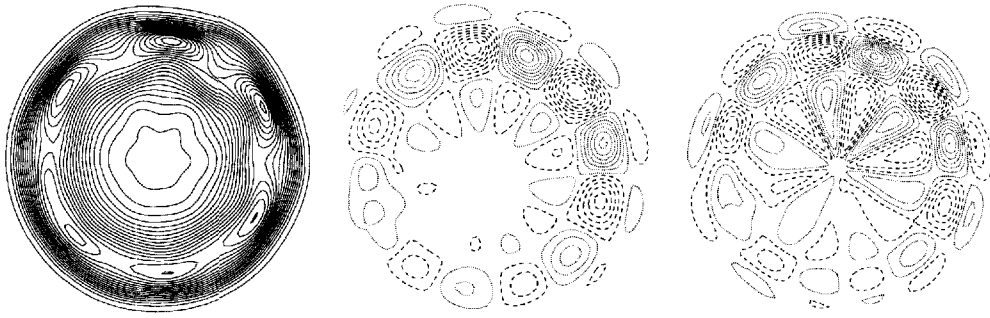

FIGURE 2. Vorticity components at $t = 70$ in the (r, θ) plane of maximum $|\boldsymbol{\omega}|$. For ω_r and ω_z dashed and dotted lines represent positive and negative values, respectively. (Case 1).

The value of e is obtained from an estimate in S78:

$$e = \frac{3\Gamma}{16\pi R^2}\left[\log\left(\frac{8R}{a_e}\right) - \frac{17}{12}\right]. \tag{3.16}$$

The parameter Re_S also governs the effect on the instability of viscous spreading of the mean flow, i.e. the instantaneous growth rate, α, can be evaluated using the locally frozen core provided it is much larger than the viscous spreading rate:

$$\frac{\alpha}{(1/\sigma)\mathrm{d}\sigma/\mathrm{d}t} = \frac{\alpha\sigma^2(t)}{2\nu} \gg 1. \tag{3.17}$$

Owing to viscous damping or wave rotation in the strain-free case, the growth rate will typically be smaller than e; hence for (3.17) to hold it is necessary that $Re_S \gg 1$.

4. Results

4.1. *Gaussian basic state; random perturbations*

In the first case, the perturbation $g(\theta)$ is specified as a sum of Fourier modes with unit amplitude and random phases (Case 1).

After some time a distinct pattern emerges (figure 2). Contours of azimuthal vorticity (ω_θ) most resemble flow visualization experiments. The $n = 6$ wave is dominant and it has the tell-tale signature of the second radial mode consistent with flow visualization experiments: for instance at a section where contours in the inner core are displaced towards the coordinate axis, contours in the outer core (both closer to and farther away from the coordinate axis) are displaced outward. In the axial and radial components the signature of the second radial mode is three layers arranged radially. The two components are in phase in each layer, suggestive of vortex lines inclined to the direction of propagation, and there is a phase shift of $0 = \pm\pi/n$ between adjacent layers. At early times the peak axial and radial vorticities grow together while the peak azimuthal vorticity decreases slightly, For $t > 70$ the axial component dominates the radial, an indication of axially elongated structures to be discussed later, and the axial component begins to grow.

In figure 3 is displayed the evolution of the energy E_n in different azimuthal modes through three phases: transient, normal mode and early nonlinear. Modes $n = 2$ and 3 continue to have oscillatory behaviour, probably because the smallness of their growth rates relative to the time scale of axisymmetric core unsteadiness allows them

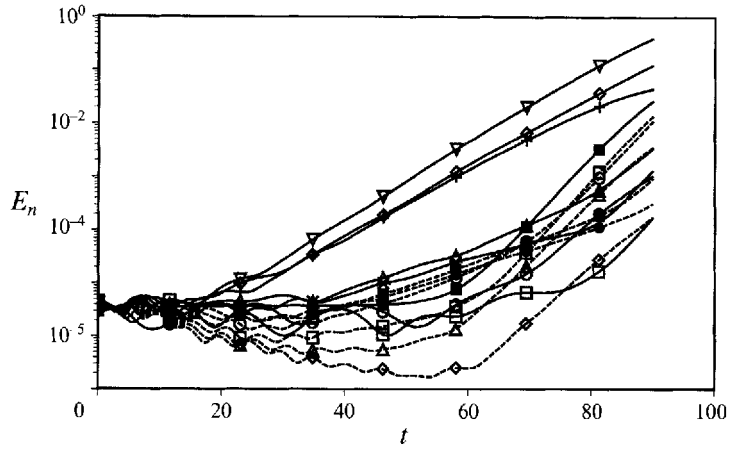

FIGURE 3. Evolution of modal energies (Case 1). ——— , $n = 1$ to 8: ■ , 1; ○ , 2; □ , 3; △ , 4; ◇ , 5; ▽ , 6; + , 7; × , 8. - - - - , $n = 9$ to 14: ● , 9; ■ , 10; ○ , 11; □ , 12; △ , 13; ◇ , 14;

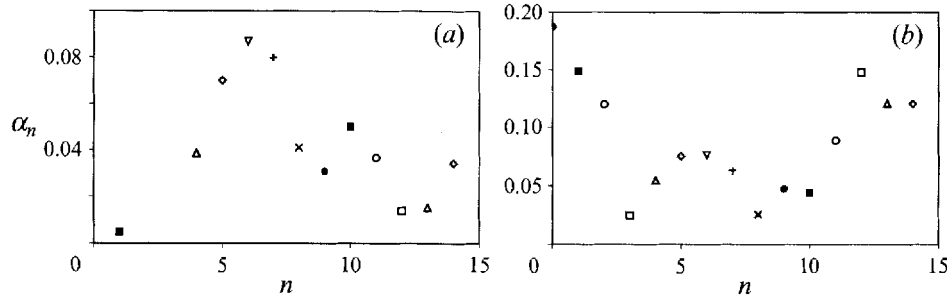

FIGURE 4. Growth rates for Case 1. (*a*) For the total energy at $t = 45$. Modes $n = 2$ and $n = 3$. have oscillatory behaviour and are not shown. (*b*) For the energy in the azimuthal velocity component at $t = 75$.

to be forced by the unsteadiness. The mean mode ($n = 0$) is not shown but has an energy of 10^2 which decreases slightly in time.

Growth rates, $\alpha_n = 1/(2E_n)(\mathrm{d}E_n/\mathrm{d}t)$, evaluated at $t = 45$ when linearly growing eigenmodes have begun to dominate over transients, are shown in figure 4(*a*). Two bands of growing waves centred about $n = 6$ and 10 are observed. As a means of reviewing some basic concepts, let us understand this by considering the heuristic picture of WBT for the linear instability according to which the growth rate is estimated as

$$\alpha = (e^2 - \Omega^2)^{1/2}, \tag{4.1}$$

where Ω is the rotation rate of waves in the unstrained rectilinear vortex. One must resort to the heuristic model because the full stability analysis involves a non-separable two-dimensional eigenvalue problem. Figure 5 plots the rotation rate (divided by core vorticity) for bending waves on a rectilinear vortex of uniform vorticity (Kelvin 1880). The term 'bending' refers to modes in which the axis of the vortex is displaced into a helix. Each curve represents a mode with a different number of zero crossings as a function of distance from the core centre: the mode labelled '0' has no zero crossings and is called the mode of pure bending, the mode labelled '1' has one zero crossing and is referred to as the second radial mode and so on. A ring can support only an

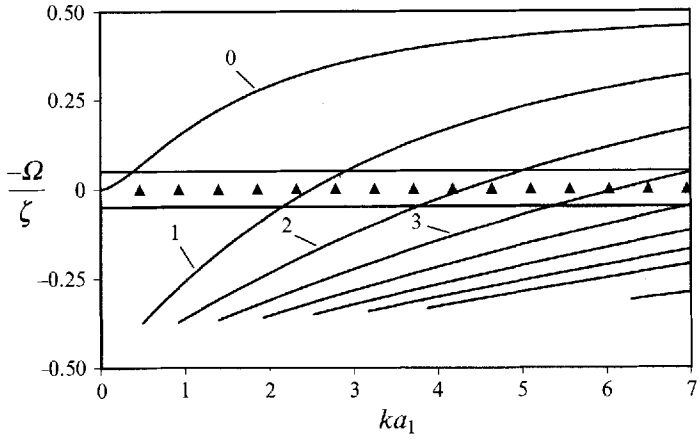

FIGURE 5. The application of the heuristic model to predict the behaviour for Case 1. See text for description.

integer number of waves, n, such that $ka_1 = (a_1/R)n$ and these values are indicated by the triangles. The two horizontal lines represent the strain rate: modes having rotation rates bounded by these lines should be unstable according to (4.1). Thus we see that there are groups of unstable waves: $n = 5$ and 6 should be unstable to a second radial mode with $n = 5$ dominant, $n = 9$ and 10 should be unstable to a third radial mode, etc. † Thin rings may display unusual behaviour: since the height of the horizontal lines $\sim O(a_1^2/R^2)$ while the spacing between the discrete modes is $O(a_1/R)$, the probability of finding an unstable mode becomes smaller for thin cores. For instance, it is possible that there are no unstable second radial modes but unstable third radial modes do exist.

The simulation result shows two, albeit wider, bands of linearly unstable waves. To ascertain the character of each wave, mode shapes of the radial vorticity are plotted (figure 6). There are qualitative similarities with the predictions of the heuristic model. One observes a group of waves ($n = 4$–8) with the structure of the second radial mode which has two nodal lines in the radial direction and a group of waves ($n = 9$–12) which are third radial modes with four nodal lines. All modes (except for $n = 13$) have the form one should expect from two-dimensional eigenfunctions, namely, they should be roughly even about the core centre.

Growth rates in the nonlinear phase are shown in figure 4(*b*). The azimuthal component of energy was chosen because it illustrates the rapid development of a mean ($n = 0$) azimuthal flow. Owing to the type of perturbation applied, the energy in this mode is initially zero but it begins to amplify steadily from the round-off threshold at about $t = 50$. Its energy at $t = 75$ is still very low [$O(10^{-9})$]. Figure 7(*a*) illustrates that it has the form of opposing streams necessary to conserve angular momentum. The next most nonlinearly amplified wave at $t = 75$ is the $n = 1$ wave. It is linearly neutral but at $t = 90$ it is the dominant of the nonlinearly amplified waves. Its mode shape (with three layers in figure 7) indicates that it results from an interaction of two second radial modes and the growth rate of its total energy at $t = 75$ is the sum of the growth rates of modes $n = 6$ and 7. This mode causes

† For clarity, the family of modes having the opposite sense of twist have been omitted in figure 5. Weak instabilities may result at the $\Omega \neq 0$ crossing points of the two families (Widnall & Tsai 1977).

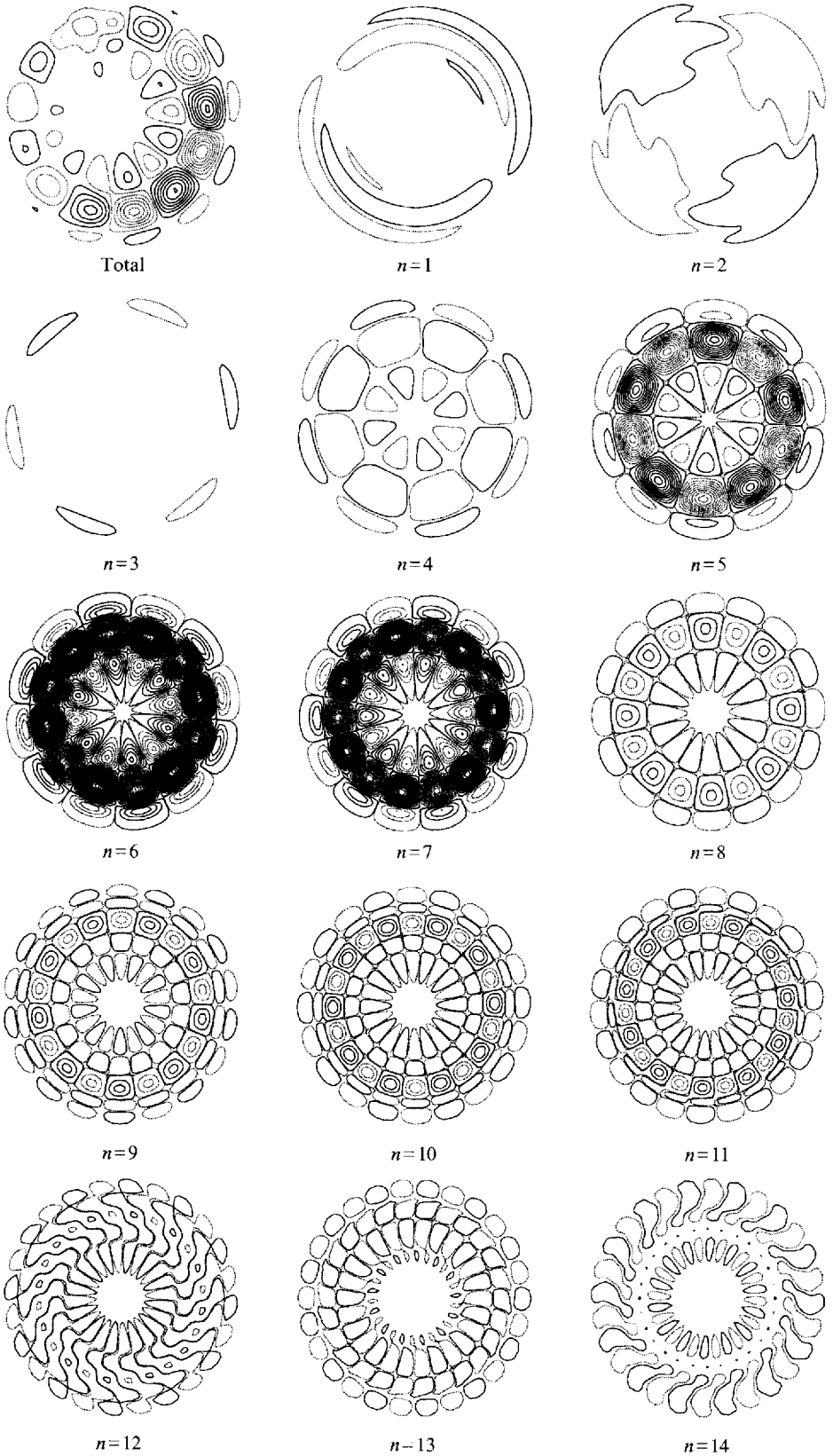

FIGURE 6. For caption see opposite

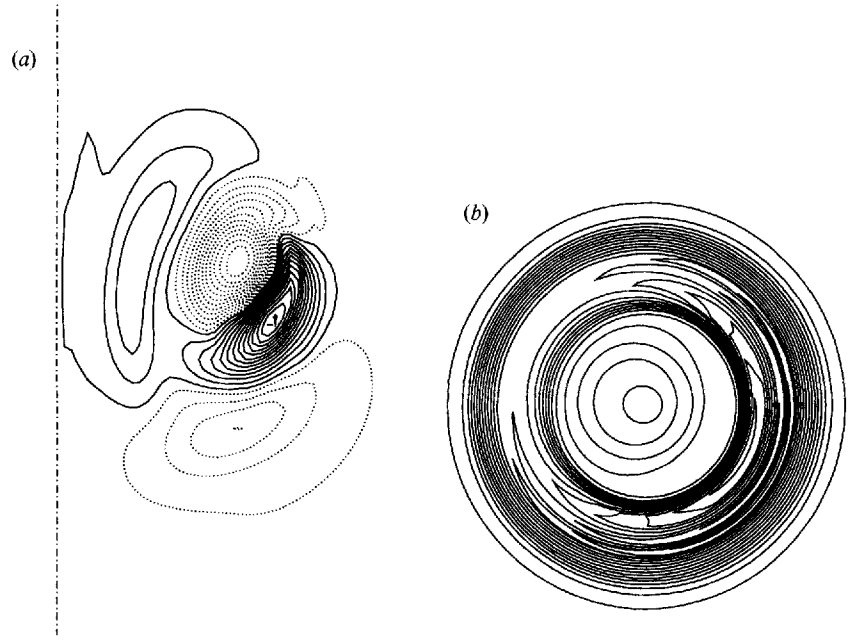

FIGURE 7. (*a*) Mean azimuthal velocity at $t = 90$. The ring motion is downward: ——— , in the direction of mean azimuthal vorticity; ····· , opposite to the mean azimuthal vorticity. Contour increment $= 5 \times 10^{-5}$. (*b*) Vorticity magnitude for superposition of the mean ($n = 0$) and $n = 1$ modes ($t = 90$). The section is the one of maximum (total) $|\boldsymbol{\omega}|$. Contour increment $= 0.10$.

contours of $|\boldsymbol{\omega}|$ to be alternately compressed and expanded in r (figure 7*b*). After the instability waves break Maxworthy (1977) observed the pulsed motion of dye in the azimuthal direction accompanied by a pulsation in core diameter. From this he inferred the presence of a single bulge wave which propagates in the azimuthal direction at a speed comparable to circumferential velocities in the core. The rapidly developing mean swirl and $n = 1$ modes may be precursors of these features.

The next most amplified wave is $n = 12$, the harmonic of the most linearly amplified mode. As nonlinearity proceeds, all mode shapes except for the primary ones (5, 6 and 7) take on a 'sheared' appearance indicative of the appearance of secondary extrema in their radial behaviour. For instance figure 8 shows the mode shape for $n = 4$. Its form is consistent with its original second radial mode structure superposed (with an angular phase difference) on a structure created from a nonlinear interaction involving one or more third radial modes.

4.2. *Viscous effects on the growth rate*

The growth rate of the theory (0.1092) is larger than the peak growth rate of the simulation. Several factors may account for this difference: (i) The theory assumes a non-rotating wave whereas it is unlikely that a wave will have exactly the value of ka_1 required for this to be true. In general waves will be rotating in the strain-free case and the growth rate will be reduced. (ii) The theory is valid for thin cores and correction terms may be significant for the thick core of the present run. (iii)

FIGURE 6. Mode shapes of the radial vorticity (Case 1, $t = 60$). Contour increment is 0.025 for the total and 0.002 for the rest. To bring this figure into the same orientation as the rest, rotate the page 90° counter-clockwise.

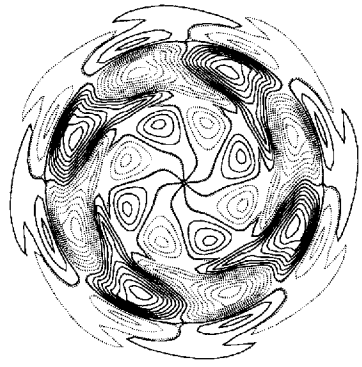

FIGURE 8. Radial vorticity for the $n = 4$ mode at $t = 90$. Contour increment $= 2 \times 10^{-3}$.

The difference in assumed vorticity distributions is not satisfactorily accounted in the growth rate by the effective core size a_1. (iv) There is a viscous correction.

This section demonstrates that (iv) accounts for most of the difference. Consider the one-term correction for the growth rate about its inviscid value α_0:

$$\alpha(\beta) = \alpha_0(\beta)\left(1 - \frac{\alpha_1(\beta)}{Re_S}\right), \tag{4.2}$$

where $\beta = a_1/R$. The regular perturbation form is valid provided there are no critical layers. It is not obvious what this means for a non-separable eigenvalue problem but by analogy with circular streamline flow one might say that there are no critical layers away from the neutral point and near the neutral point provided the angular phase velocity of the wave is nowhere the same as the angular velocity of fluid particles. If (4.2) is valid up to the point of damping then $\alpha_1(\beta)$ is the critical Reynolds number for the mode. We will see that the choice Re_S for the Reynolds number makes $\alpha_1(\beta)$ least sensitive to β.

In the simulations normal-mode behaviour is present in a certain window of time in which for different Γ/ν the basic flow has spread by different amounts. This forces us to consider the viscous correction in two ways. The first serves to describe the simulation results but cannot be readily used outside of this work for quantitative or modelling purposes. The second is more fundamental but only scant information can be obtained from the simulations. The first viewpoint considers the growth rate at fixed time t (normalized by Γ and R) for a fixed wavenumber n with the parameters Re_S and β referred to $t = 0$. Hence, the effects of both viscous damping as well as the shift in $ka_1(t)$ as a_1 grows are observed. The second viewpoint considers the instantaneous growth rate of a fixed-ka_1 mode with parameters Re_S and β referred to the present. This is closer to the type of information a viscous stability analysis would provide. Using (4.1) it is not difficult to show that for an initially non-rotating wave ($\Omega(0) = 0$), the decrease in growth rate from its value at the initial instant to its value at time t which comes about due to core spreading is $O(1/Re_S{}^2)$. This partly accounts for the agreement we will observe for the most amplified wave between results adopting the two viewpoints. On the other hand if $\Omega(0) \neq 0$ the decrease or increase in growth rate is $O(1/Re_S)$.

Figure 9 presents results adopting the first viewpoint. It plots growth rate scaled by the WT value for the second or third radial mode, as appropriate, for several n and different initial Reynolds numbers. The growth rates are obtained as an average

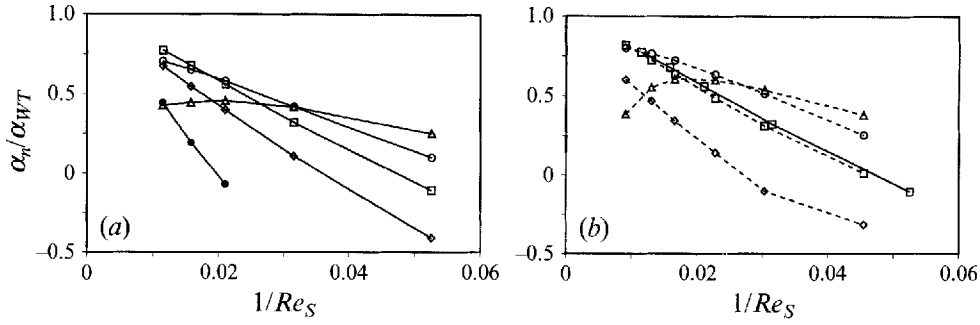

FIGURE 9. Viscous effect on growth rates of selected modes. (*a*) Full-core cases: △ , $n = 4$; ○ , $n = 5$; □ , $n = 6$; ◇ , $n = 7$; • , $n = 10$. (*b*) Medium-core cases: △ , $n = 6$; ○ , $n = 7$; □ , $n = 8$; ◇ , $n = 9$; -⊟- , the curve for $n = 6$ from (*a*).

between $t = 45$ and 60 for the full-core cases and between $t = 40$ and $t = 60$ for the medium-core cases. For the medium-core case at high Reynolds numbers the energy growth for the lowest n in the figure has small oscillations which disappear as the Reynolds number is decreased while oscillations and some curvature appear for the higher n. For the full-core cases, oscillations and curvature appear for the highest wavenumber at low Reynolds numbers.

First consider the full-core cases (figure 9*a*). The result for $n = 6$ (□) follows (4.2) well even up to the point of damping, with the inviscid limit being close to the WT value. Hence we rule out factors (i)–(iii) listed above as playing a large role. The levelling or decrease in the curves for $n = 5$ (○) and $n = 4$ (△) at the highest Reynolds numbers is due to core spreading: with decreasing Reynolds number, the core thickens more rapidly and these modes are closer to the non-rotating wave of the rectilinear vortex at the observation time.

To assess the effect of the parameter β, runs are performed for a core 3/4 as thick (Cases 6–11, figure 9*b*). According to the heuristic picture the mode with a value ka_1 closest to the non-rotating second mode is the most unstable. Therefore given that $n = 6$ is the most inviscidly amplified wave for the full core, we expect either $n = 7$ or 8 or 9 to be the most inviscidly amplified wave here. We see from figure 9(*b*) that $n = 8$ (□), the correspondent of the $n = 6$ wave of the full core is the most amplified inviscid wave. For this mode values for α_1 range between 20.0 and 22.8. This is not too different from the range (19.7–21.1) for $n = 6$ in the full-core cases. On the other hand the dependence is more sensitive if Γ/ν is used as the Reynolds number: then the range of α_1 is 1244–1328 for the full-core cases and 1818–2069 for the 3/4 core. As one would expect, for the same value of Γ/ν the magnitude of the viscous correction is larger for a thinner core. Similarly if Re_D is used the ranges are 476–509 for the full core and 779–887 for the 3/4 core. It may be worth noting that Glezer's (1988) transition map (his figure 6) for turbulent rings immediately after ejection displays the opposite trend, namely, higher L/D_e ratios have a higher critical Γ/ν, suggesting that the transition mechanism there is quite different.

Finally, note that while the second and third radial modes ($n = 10$, figure 9*a*) have nearly identical inviscid growth rates, viscosity damps the third mode faster. Symbols for the two lowest Reynolds number cases are omitted since the mode is highly damped and normal-mode behaviour is not discernible.

With respect to the second viewpoint, a complete mapping of the parameter space is not possible from the available simulations since in the period of normal-mode

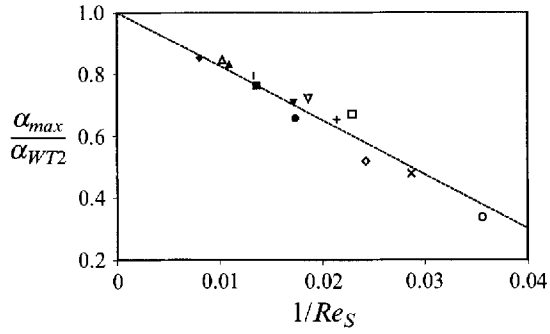

FIGURE 10. Growth rates of the most amplified wave for the Cases 1–13. Re_S was evaluated at the instant the growth rate was computed. Cases: △, 1; ■, 2; ●, 3; ◇, 4; ○, 5; ◆, 6; ▲, 7; |, 8; ▼, 9; +, 10; ×, 11; ▽, 12; □, 13. ---- , $1 - 18/Re_S$.

Case	Most amplified n expected $n(0), n(45), n(90)$	Most amplified n observed at $\bar{t}$	$\bar{t}$	$a_1(\bar{t})/R$	Dominant n
1	5,5,5	6	52.5	0.51	6
2	5,5,5	6	52.5	0.53	6
3	5,5,4	5	52.5	0.55	6, 5 ($t = 65$)
4	5,4,4	4	52.5	0.59	5
5	5,4,4	4	57.5	0.68	4
6	7,7,6	8	52.5	0.38	8, 7 ($t = 78$)
7	7,6,6	7	52.5	0.40	8,7 ($t = 57$)
8	7,6,6	7	52.5	0.41	7
9	7,6,5	7	52.5	0.43	7
10	7,6,5	6	52.5	0.46	7
11	7,5,4	6	52.5	0.50	7, 6 ($t = 39$)
12	11,8,7	9	52.5	0.32	10,9 ($t = 80$)
13	11,8,6	8	52.5	0.35	10,9 ($t = 51$),8 ($t = 86$)

TABLE 4. Most amplified and dominant wavenumbers

behaviour the values of ka_1 for the different n, the values of Re_S and a_1/R differ widely. Therefore we shall focus only on the most amplified mode. Figure 10 plots for each of the 13 cases the value of α/α_{WT2} for the most amplified wave with Re_S evaluated at the instant the growth rate is computed (more precisely, at the mid-point, $\bar{t}$, of an averaging interval of width $\Delta t = 15$), assuming the spreading law (12). The corresponding values of $a_1(\bar{t})/R$ and n are given in table 4.

Despite differences in a_1/R and n, the data are approximated well by the line $1 - 18/Re_S$. It should be noticed that if the most amplified n is the one closest to the inviscid non-rotating wave, then the values of na_1/R must lie between $2.51 \pm a_1/(2R)$. This fails to be true in many cases (most prominently for Case 2) and its cause is not understood.

In a spectral simulation of the Widnall instablity in a triply periodic cube, Hasselbrink (1992) observed that the dominant number of waves indicated by surface contour plots switched in time from 9 to 8 and then to 7 and found that the corresponding value of $k\sigma(t)$ increases away the value for the second radial mode but returns close to it after each switch. The switching phenomenon is also present here.

The last column of table 4 shows the most energetic mode; times at which switchings occur are shown in parenthesis. Note the expected delay in some cases between the time when a mode is most amplified and the time at which it becomes dominant. A unit change in the number of waves has no experimental precedent to our knowledge.

The result that Re_S is the appropriate Reynolds number and the value of the coefficient α_1 is consistent with the effects of viscosity on a two-dimensional flow with elliptical streamlines (Landman & Saffman 1987, hereafter LS). First, make the assumption (to be checked below) that the regime of the elliptical flow appropriate to even rather thick vortex rings is one of small $\beta_{LS} \equiv \epsilon_{LS}/\gamma$. Here ϵ_{LS} is the rate of strain in the elliptical flow and γ is half the value of the vorticity, which is uniform. We are employing the same symbols as Landman & Saffman, using the subscripts LS to distinguish them from our symbols only where necessary. Correspondence between this flow and an isolated elliptical vortex patch with imposed strain is obtained by matching streamline aspect ratio, λ. For small strain one has $\epsilon_{LS}/\gamma = \lambda - 1$ in the former case and $2e/\gamma = \lambda - 1$ in the latter so we identify ϵ_{LS} with $2e$. That this is valid is also indicated by the fact that the peak growth rate is $(9/16)\epsilon_{LS} + O\epsilon_{LS}^2$ for the elliptical flow (Waleffe 1989) but nearly e for the elliptical patch (Robinson & Saffman 1984). Hence we take $\beta_{LS} = 4e/\zeta$ where $\zeta = \Gamma/(\pi a_1^2)$ is the 'average' vorticity in the vortex ring.

Figure 2 in LS provides the critical value of E_γ (an inverse Reynolds number), above which all modes are stable (for small β_{LS}):

$$E_\gamma \equiv \frac{2\pi\nu k_o^2}{\gamma} \approx 3.25\beta_{LS} - c_1\beta_{LS}^2 + O(\beta_{LS}^3), \tag{4.3}$$

where k_o is the wavenumber of the most amplified disturbance and c_1 is a positive constant included to point out the downward deviation from the leading behaviour. For the thickest vortex ring simulations we have $4e/\zeta = 0.2$ and figure 2 in LS shows that the leading term in (4.3) is still quite accurate. Dividing (4.3) by β_{LS} transforms E_γ to something $\propto 1/Re_S$ and eliminates the leading order dependence on β_{LS}. In particular, putting the axial wavenumber $k = k_o \cos\theta_{LS}$ with $\theta_{LS} = \pi/3 - c_2\beta_{LS} + O(\beta_{LS}^2)$ ($c_2 \approx 0.24$ from figure 3 in LS) and using $ka_1 = 2.51$ for the second radial mode we obtain for the critical value of Re_S

$$(Re_S)_c = 24.4\left[1 - (3.5c_2 - .31c_1)\beta_{LS} + O(\beta_{LS}^2)\right]. \tag{4.4}$$

The leading-order term compares reasonably with the value (≈ 18) obtained from the vortex ring calculations. If we put $ka_1 = 4.35$ for the third radial mode, the leading factor is changed to 73.2 which should be compared with the value (≈ 50) observed from the vortex ring simulations. It should also be noted that the one-term viscous correction is exact in the elliptic streamline flow.

The time or location at which initial waviness and breaking is observed in the laboratory, although dependent on the judgement of the observer, is the only available diagnostic related to the growth rate. Liess & Didden (1976) provide time measurements for $L/D_e = 1.4$ which indicate slowing of the instability as the piston Reynolds number, Re_p, is decreased. At first glance, this would seem to be a result of the viscous correction. The situation is more complicated, however. As mentioned earlier, Re_p affects the initial and developing core structure and this can alter the *inviscid* growth rate. Consider a model in which the inviscid growth rate is used and the effect of Re_p on the core structure is accounted for by allowing the value of $\hat{\epsilon}$ to obey (3.14). An equation for the number of e-folds is evolved with initial conditions

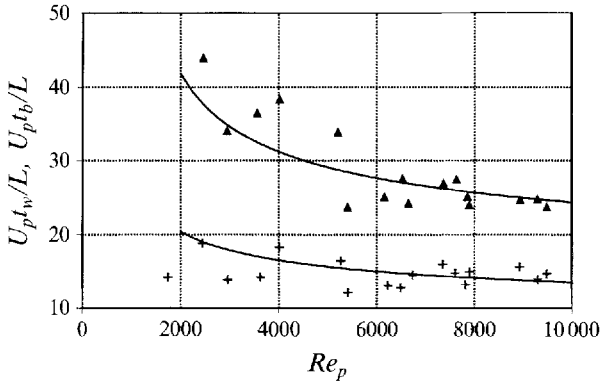

FIGURE 11. Time when waviness appears (t_w) and when the wave breaks (t_b). +, Liess & Didden (1976) data for t_w; ▲, data for t_b; ———, model with $e_n = 8.25$ and 14 for the lower and upper curves, respectively.

specified at the end of the piston motion:

$$\frac{\mathrm{d}e_f}{\mathrm{d}t} = \alpha(t), \qquad e_f(L/U_p) = 0, \tag{4.5}$$

where $\alpha(t)$ is calculated using (3.7) and $a_1(t)/R$ and is obtained from (3.9)–(3.11). Times are recorded when e_f reaches specified values e_n. The prediction of the model reasonably follows the experimental data (figure 11). Hence the presence of a direct viscous effect on the instability cannot be inferred from the behaviour with Re_p.

A referee suggested that we critically compare the experimentally observed dominant n with existing models and the current results. Early experiments (Widnall & Sullivan 1973) present the number of waves as a function of a non-dimensional ring speed parameter, $\widetilde{V}$, in order to bring out the connection with inviscid theory. However, Liess & Didden (1976) observed that with $\widetilde{V} = 3$ and $L/D = 1.4$ (both fixed), n increased from 5 to 11 as Re_p was increased. Maxworthy (1977) found the increase to be unabated at higher Re_p. Saffman (1978) showed that this is due to the fact that as Re_p is varied the following change: (i) the shape (peakiness) of the initial vorticity profile and (ii) the rate of viscous growth of the core size. A third change might be a slight shift in the most-amplified ka_1 with viscosity which manifests as a shift in θ_{LS} in the elliptic streamline flow. The present medium-core simulations cover the same range of Re_p as the Leiss & Didden (1976) data and have a similar value of L/D_e (= 1.53) but n varies from 6 to 8 only (table 4). This is because only effect (ii) is present in the simulations. Saffman's estimates based on both effects reproduce the experimental data astonishingly well but there is room for improvement. Saffman assumed the dominant n to be given by the instantaneously most amplified inviscid mode, the instant being chosen such that $Re_S = 60$, a critical value chosen to fit experiments. In reality one should track the time-varying amplitude growth of each n separately and determine which reaches a critical amplitude first. The instantaneous growth rate should account for changes in the inviscid growth rate as the core grows, viscous corrections and wave rotation in the unstrained vortex. The elliptic streamline flow has all the ingredients necessary to build such a model.

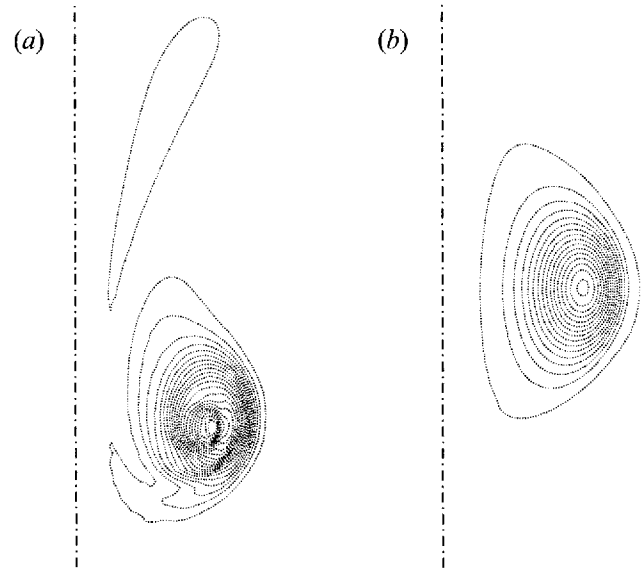

FIGURE 12. Azimuthal vorticity at $t = 20$ in the meridional section of maximum $|\boldsymbol{\omega}|$. The ring motion is downward. (*a*) Gaussian initial condition; (*b*) equilibrated initial condition. Contour increment is 0.1.

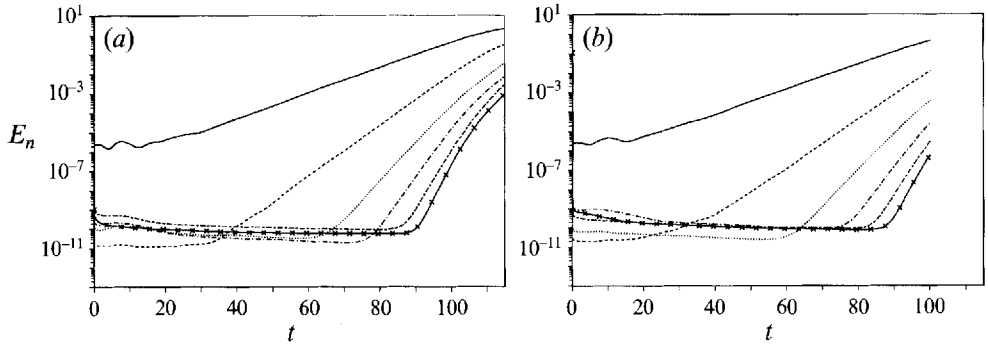

FIGURE 13. Evolution of modal energies for cases with an $n = 5$ perturbation. $|\boldsymbol{\omega}|$. (*a*) Gaussian initial condition; (*b*) equilibrated initial condition. ——— , $n = 5$; - - - - , $n = 10$; ····· , $n = 15$; —·— , $n = 20$; — - — , $n = 25$; -×- , $n = 30$;

4.3. *Equilibrium/Gaussian basic states; n = 5 perturbation*

While a random perturbation corresponds better to the experimental situation, vorticity dynamics and some aspects of nonlinear mode interactions are better understood when only selected modes are initially excited. In the present case, the initial perturbation consists of a single azimuthal wavenumber ($n = 5$) known to be linearly amplified from Case 1 with random perturbations. The computation is performed in a fifth of the domain, allowing greater resolution.

Figure 12 shows the azimuthal vorticity after roughly two eddy turnover times for the Gaussian and equilibrated basic states. The former case is undergoing axisymmetric adjustment and a tail has been shed in which one should expect axial vorticity to be intensified. Yet figure 13 shows that except for small differences during the transient and slightly delayed onset of the normal-mode behaviour, the two cases

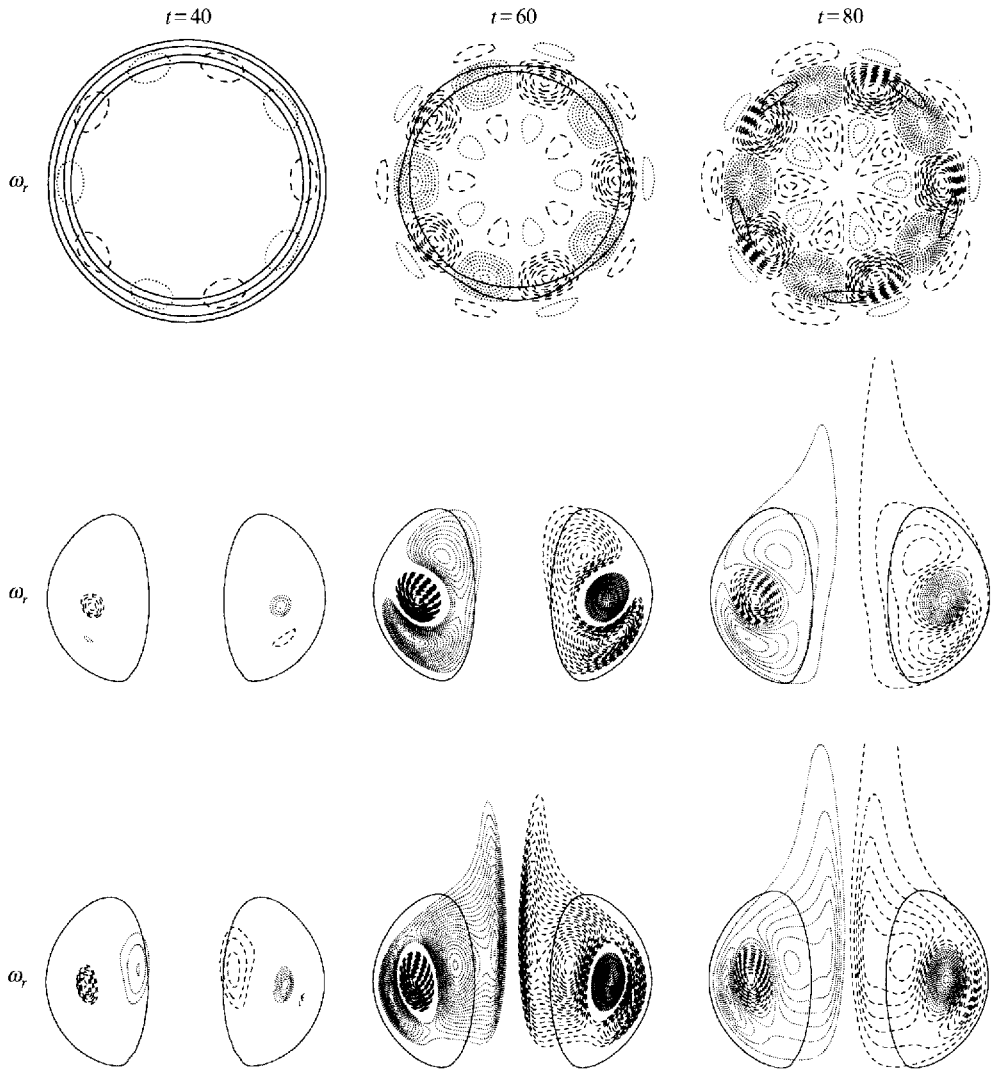

FIGURE 14. Vorticity field for Case 15 ($n = 5$ perturbation, equilibrated). The solid line represents azimuthal vorticity in all plots. The other component plotted in each row is indicated on the left and dashed/dotted lines represent its positive/negative values. Contour increment for ω_r and ω_z is 0.005 at $t = 40$ and 60 but 0.015 at $t = 80$.

have very similar energy histories. Contour plots also indicated minor differences. It may be that at higher Reynolds numbers the tail shedding could lead to a 'bypass' transition. The growth rate is $\alpha = 0.074$ (equilibrium case) which agrees well with the value obtained with random perturbations.

Figure 13 shows that the $n = 10$ harmonic starts growing exponentially due to nonlinearity when the fundamental reaches a certain amplitude. Thereafter higher harmonics begin to grow with progressively higher exponential rates. Nonlinear growth rates scale almost perfectly with n indicating that higher harmonics are created by products of lower harmonics.

An effect of curvature is that whereas for a rectilinear vortex in a strain field there is no preferred direction for nonlinear steepening of the wave, here one observes that

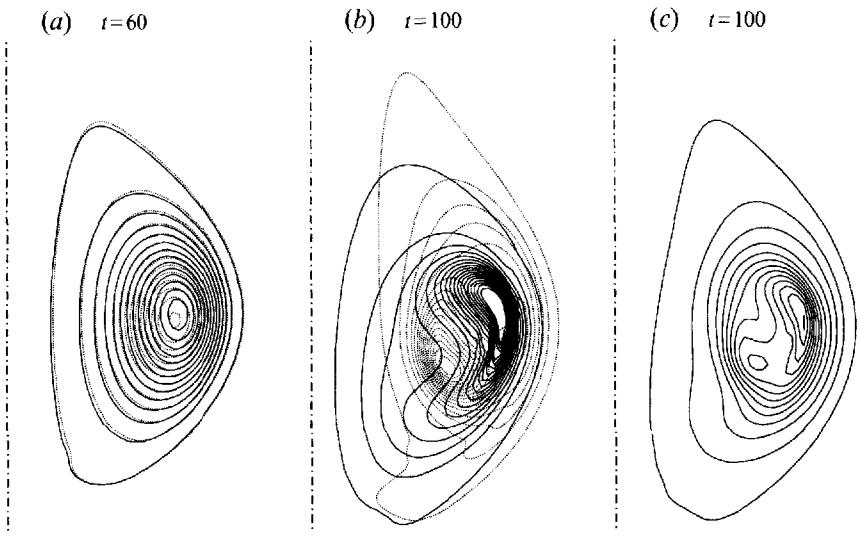

FIGURE 15. Azimuthal vorticity for Case 15 ($n = 5$, equilibrated initial condition). The ring motion is downward. (*a*, *b*) Azimuthal vorticity at the meridional sections $\theta = 0$ (solid) and $\theta = 2\pi/10$ (dotted) at which there is maximum and minimum radial displacement of the core, respectively. (*c*) Azimuthal mean of azimuthal vorticity. Contour increment is 0.1 in all plots.

elongation takes place behind the ring and a wake of mostly axial vorticity is shed. This is shown in figure 14 in which contours of radial (middle row) and axial (bottom row) vorticity are shown in a meridional plane. The shed vorticity originates from the inner of the three layers of the second radial mode and its waviness is shifted by $\theta = \pi/5$ relative to the waviness of the ring core, i.e. where the inner core has positive axial vorticity it is enveloped in the outer core by negative axial vorticity which extends into the wake forming one leg of a 'hairpin' vortex and similarly with the signs reversed. This may be the first step of the process, observed through dye visualization, in which rings having become turbulent following the wavy instability eject hairpin shaped dye filaments at regular intervals (Schneider 1980; Auerbach 1991). The recent measurements of Weigand & Gharib (1994) indicate that the ejected fluid is indeed vortical.

Because Maxworthy (1977, p. 482) has experimentally observed a non-rotating wave at roughly 45° initially and notes that it only begins to rotate at large amplitude just prior to the creation of turbulence, the 'angle of the instability wave' as deduced in an experiment is of particular interest. It should be noted that the linear eigenmode increases in amplitude with a fixed form but in experiments it is the core displacement which is being visualized, hence the use of the quotes above. This angle is obtained in figure 15 by superimposing contours of total azimuthal vorticity at the meridional sections of maximum and minimum radial displacement of the core (solid and dotted lines respectively). The angle of the line joining the peak of the solid contours to the peak of the dotted contours gradually increases from zero to about −42° relative to the direction of propagation; the sign is consistent with the direction of positive strain. Owing to loss of resolution soon after the last instant shown, we are unable to enter the period in which rotation might be occurring.

The mean flow changes considerably from its initial form. Figure 15(*c*) shows the azimuthal mean of the azimuthal vorticity at the last instant (other mean vorticity components are $O(10^{-6})$). It has two concentrations at the angle of waviness previ-

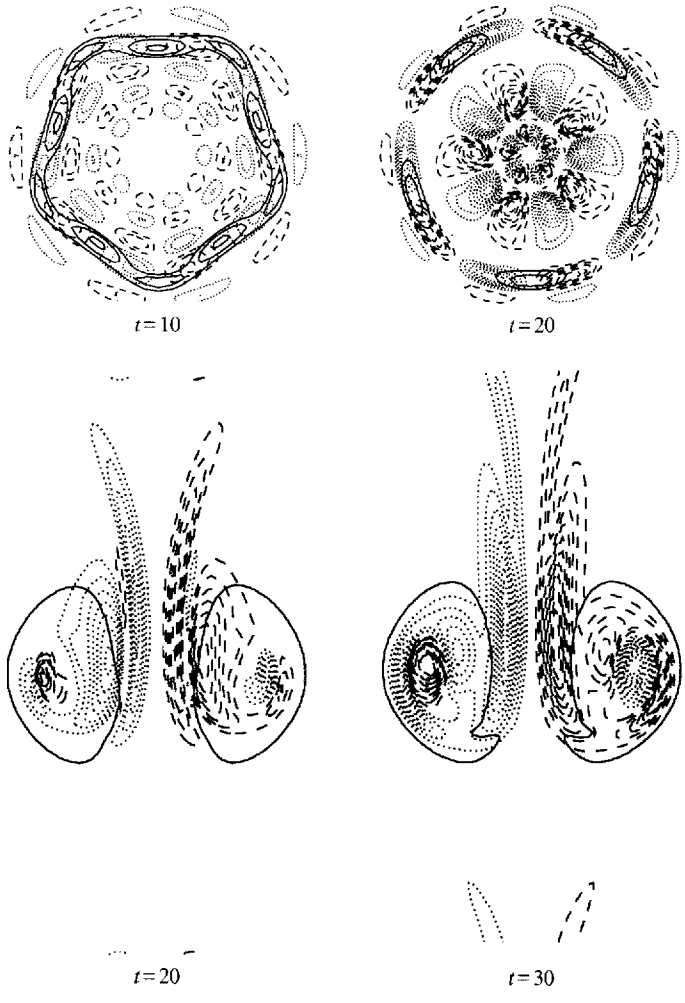

FIGURE 16. Vorticity field for the large-perturbation run (Case 16): ——— , azimuthal vorticity (contour increment = 0.1); ····· , – – – – , positive and negative axial vorticity, respectively (contour increment = 0.05).

ously obtained. If the wave were to begin rotating, an unsteady mean vorticity with a long-range Biot–Savart induced velocity would develop leading to stretching and folding of the shed vorticity. This might be next step in the transition process.

4.4. *Large perturbation case* ($\epsilon = 0.02$)

Here we brifely consider the case of a large initial perturbation which can be thought of as having arisen from other instability mechanisms active during ring formation or after nonlinear saturation. To eliminate effects of axisymmetric tail shedding the equilibrated initial condition is used.

Figure 16 shows that a higher radial mode with five radial layers is excited after one eddy turnover period ($t = 10$). In each layer the axial vorticity is phase shifted π/n relative to the adjacent layer. At $t = 20$ the fourth layer (counting from large to small r) has almost dissipated. Note the difference in the structure of the wake compared with the small-perturbation case (figure 14). This wake structure is reminiscent of the dye visualization photographs of Glezer (1988, figure 9) of a turbulent vortex

ring being formed at a generator and also of the descriptions of Auerbach (1991) of a turbulent vortex ring in which periodic ejections of hairpin vortices into the wake were observed. In early experimentation with different forms of the initial perturbation even more layers with greater persistence were observed (e.g. 7 layers at $t = 40$). Examination of modal energies indicates that the harmonic $n = 10$ is nonlinearly amplified from the outset but the fundamental has a linear growth with a smaller growth rate than the small-perturbation case.

Finally, we would like to mention Cases 17 and 18 in which both grid and time step were refined a little and energy histories were plotted for the $n = 5$ and $n = 10$ modes with identical results.

5. Closing remarks

With respect to the three goals set in the introduction the present work has merely addressed the linear and early nonlinear phases of the instability and finds the following.

(i) The existence of linearly unstable bands and their modal structure is in general agreement with the inviscid heuristic picture of Widnall, Bliss & Tsai (1974).

(ii) There is a viscous correction factor to the inviscid growth rate which is well described by $1-\alpha_1/Re_S$ even up to the point of damping. The Reynolds number, Re_S, defined by Saffman (1978) and based on strain rate due to curvature is appropriate because it makes α_1 insensitive to the core size ($\alpha_1 \approx 20$ for the second radial mode). These results are consistent with the behaviour of the elliptic streamline flow (Landman & Saffman 1987).

(iii) In the nonlinear stage there is (*a*) amplification of mean swirl and the $m = 1$ wave which arises from the interaction of neighbouring second-mode waves; (*b*) a modified mean azimuthal vorticity with a double peak; (*c*) elongation of the inner layer of the most linearly unstable mode towards the rear of the ring.

We look forward to investigating the later stages of transition. Maxworthy's (1977) observations lead one to expect that the instability wave will begin to rotate and that the nonlinearly growing mean swirl and $n = 1$ modes will develop into a rapidly propagating bulge wave. The observations of Schneider (1980), Auerbach (1991) and Weigand & Gharib (1994) lead one to expect that a periodic ejection of hairpin vortices into the wake will take place.

In contrast to Maxworthy's observations of the growth and breaking of instability waves, Sturtevant's (1981) schlieren observations of high Reynolds number thin rings generated in a shock tube showed that the waves decay and vanish without breaking! He attributed this difference to the visualization technique used, in particular to the fact that the schlieren technique provides a better instantaneous picture of the vortex core than dye whose pattern is influenced by the history of the motion. His explanation for the phenomenon is that at later times the vorticity becomes redistributed to create a stable ring.

He observed that for shorter lengths of the driver section of the shock tube (hence thinner rings) the waves decayed faster as a function of propagation distance. Indeed for the shortest driver the instability failed to appear. The trend with core thickness suggests viscous damping but an estimate shows that the experimental $Re_S \geqslant 45$, which makes this explanation unlikely. (The estimate is made by obtaining a_1/R from the number of observed waves, which gives Re_S/Re_D. The range of Re_D is obtained from the range of drift velocities reported by Sturtevant.)

The authors express gratitude to Professors S.K. Lele and T.S. Lundgren for useful discussions. Most of the simulations were carried out at NASA-Ames to which authors express their gratitude. The research was partially supported by a grant from Agenzia Spaziale Italiana under contract No. ASI92RS27/141ATD.

REFERENCES

AUERBACH, D. 1991 Stirring properties of vortex rings. *Phys. Fluids* A **3**, 1351–1355.

BAYLY, B. J. 1986 Three-dimensional instability of elliptical flow. *Phys. Rev. Lett.* **57**, 2160–2163.

BRASSEUR, J. G. & CHANG, I.-D. 1980 Combination of kinematics with flow visualization to compute total circulation. *AIAA J.* **19**, 878–884.

COUDER, Y. & BASDEVANT, C. 1986 Experimental and numerical study of vortex couples in two-dimensional flows. *J. Fluid Mech.* **173**, 225–251.

CROW, S. C. 1970 Stability theory for a pair of trailing vortices. *AIAA J.* **8**, 2172–2179.

DIDDEN, N. 1979 On the formation of vortex rings: rolling-up and production of circulation. *Z. Angew. Math. Phys.* **30**, 101–116.

GLEZER, A. 1988 The formation of vortex rings. *Phys. Fluids* **31**, 3523–3542.

HARLOW, F. H. & WELCH, J. E. 1965 Numerical calculation of time-dependent viscous incompressible flow of fluid with free surface. *Phys. Fluids* **8**, 2182–2189.

HASSELBRINK, E. F. 1992 Breakdown and mixing in a viscous circular vortex ring. BS thesis, Dept. of Mech. Eng., Univ. Houston.

KELVIN, LORD 1880 Vibrations of a columnar vortex. *Lond. Edin. Dublin Phil. Mag. J. Sci.* (5) **10**, 155–168.

KIM, J. & MOIN, P. 1985 Application of a fractional-step method to incompressible Navier–Stokes equations. *J. Comput. Phys.* **59**, 308–323.

LANDMAN, M. J. & SAFFMAN, P. G. 1987 The three-dimensional instability of strained vortices in a viscous fluid. *Phys. Fluids* A **30**, 2339–2342 (refered to herein as LS).

LEITH, C. E. 1984 Minimum enstrophy vortices. *Phys. Fluids* **27**, 1388–1395.

LIESS, C. & DIDDEN, N. 1976 Experimente zum Einfluss der Anfangsbedingungen auf die Instabilität von Ringwirbeln. *Z. Angew. Math. Mech.* **56**, T206–T208.

LIN, S. J. & CORCOS, G. M. 1984 The mixing layer: deterministic models of a turbulent flow. Part 3. The effect of plane strain on the dynamics of streamwise vortices. *J. Fluid Mech.* **141**, 139–178.

MAXWORTHY, T. 1977 Some experimental studies of vortex rings. *J. Fluid Mech.* **81**, 465–495.

ORLANDI, P. 1989 Numerical simulation of vortex motion in the presence of solid boundaries. In *Proc. Eighth GAMM Conference on Numerical Methods in Fluid Mechanics* (ed. P. Wesseling), pp. 436–441. Vieweg & Sohn.

PIERREHUMBERT, R. T. 1986 Universal short-wave instability of two-dimensional eddies in an inviscid fluid. *Phys. Rev. Lett.* **57**, 2157–2159.

PIERREHUMBERT, R. T. & WIDNALL, S. E. 1982 The two- and three-dimensional instabilities of a spatially periodic shear layer. *J. Fluid Mech.* **114**, 59–82.

PULLIN, D. I. 1986 Vortex ring formation at tube and orifice openings. *Phys. Fluids* **22**, 401–403.

ROBINSON, A. C. & SAFFMAN, P. G. 1984 Three-dimensional stability of an elliptical vortex in a straining field. *J. Fluid Mech.* **142**, 451–466.

SAFFMAN, P. G. 1970 The velocity of viscous vortex rings. *Stud. Appl. Maths* **49**, 371–380.

SAFFMAN, P. G. 1978 The number of waves on unstable vortex rings. *J. Fluid Mech.* **84**, 625–639 (referred to herein as S78).

SAFFMAN, P. G. 1988 The stability of vortex arrays to two- and three-dimensional disturbances. *Fluid Dyn. Res.* **3**, 13–21.

SCHNEIDER, P. E. M. 1980 Sekundärwirbelbildung bei Ringwirbeln und in Freistrahlen. *Z. Flugwiss. Weltraumforsch.* **4**, 307–318.

STURTEVANT, B. 1981 Dynamics of turbulent vortex rings. *AFOSR-TR-81-0400.* (Available from Defense Technical Information Service, Govt. Accession. No. AD-A098111, Fiche N81-24027.)

TSAI, C.-Y. & WIDNALL, S. E. 1976 The stability of short waves on a straight vortex filament in weak externally imposed strain field. *J. Fluid Mech.* **73**, 721–733.

VERZICCO, R. & ORLANDI, P. 1993 A finite-difference scheme for three-dimensional incompressible flows in cylindrical coordinates. Submitted to *J. Comput. Phys.*

WALEFFE, F. 1989 The 3D instability of a strained vortex and its relation to turbulence. PhD thesis, Dept. of Maths, Mass. Inst. Tech.

WEIGAND, A. & GHARIB, M. 1994 The re-laminarization of a turbulent vortex ring. Submitted to *Phys. Fluids.*

WIDNALL, S. E., BLISS, D. B. & TSAI, C.-Y. 1974 The instability of short waves on a vortex ring. *J. Fluid Mech.* **66**, 35–47 (referred to herein as WBT).

WIDNALL, S. E. & SULLIVAN, J. P. 1973 On the stability of vortex rings *Proc. R. Soc. Lond.* A **332**, 335–353.

WIDNALL, S. E. & TSAI, C.-Y. 1977 The instability of the thin vortex ring of constant vorticity. *Phil. Trans. R. Soc. Lond.* A **287**, 273–305 (referred to herein as WT).

WRAY, A. A. 1987 Very low storage time-advancement schemes. *Internal Report.* NASA Ames Research Center, Moffett Field, California.